Poroelastic response of articular cartilage by nanoindentation creep tests at different characteristic lengths

M. Taffetani [a], R. Gottardi [c], D. Gastaldi [a], R. Raiteri [b], P. Vena [a,d,*]

[a] Department of Chemistry, Materials and Chemical Engineering, Laboratory of Biological Structure Mechanics (LaBS), Politecnico di Milano, Italy
[b] Department of Informatics, Bioengineering, Robotics and System Engineering, University of Genova, Genova, Italy
[c] Ri.MED Foundation, Palermo, Italy
[d] IRCCS, Istituto Ortopedico Galeazzi, Milano, Italy

Received 20 April 2013
Received in revised form 14 February 2014
Accepted 23 March 2014

1. Introduction

Articular Cartilage (AC) is a connective tissue able to grant a low friction coefficient [1] and the smoothness in the transmission of load between diarthrodial joints. AC inhomogeneous, highly anisotropic and non-linear properties are strictly related to its structure, which is in turn determined by the molecular and ultrastructural organization of its components [2].

The solid phase of AC is constituted mainly by a dense network of collagen fibrils and interspersed proteoglycans (PGs) with a sparse population of chondrocytes; the interstitial fluid phase, that saturates the solid matrix, is composed by water and free ions as Na^+, K^+, Ca^+ [3]. Since the superficial layer of AC is crucial for both its mechanical function and in damage initiation, there is a major interest in investigating the properties of the top 20% of the overall tissue thickness. The superficial layers present the higher water content, almost 80% of its wet weight, and collagen density, up to 50–75% of its dry weight. The viscoelastic properties, which are dependent on the molecular structure and its evolution under stress, and the extrinsic properties, which are dependent on the fluid flow through the porous solid matrix, exhibit mutual interaction.

In this work we are interested in the extrinsic time dependent properties of the AC tissue, governed by the fluid flow through its porous microstructure, i.e., in AC poroelasticity. Terzaghi [4] first introduced the poroelastic model for soils, assuming that both the solid and fluid phases fill homogeneously the volume, and Biot [5] extended it to a tridimensional anisotropic case; moreover, Rice and Cleary [6] highlighted the limit conditions described by drained (at equilibrium) and undrained (short term) moduli. A comprehensive description of the physics of fluid saturated solids is also available in Coussy [7]. The problem of compression of disks with anisotropic poroelasticity was solved analytically in Cowin and Doty [8]; the application of the poroelastic theory to cartilage can be found in

* Corresponding author at: Department of Chemistry, Materials and Chemical Engineering, Laboratory of Biological Structure Mechanics (LaBS), Politecnico di Milano, Italy. Tel.: +39 0223994236; fax: +39 0223994220.
E-mail address: pasquale.vena@polimi.it (P. Vena).

many papers including those by Armstrong et al. [9] and Cohen et al. [10]. The biphasic (or triphasic) models consider, instead, the different cartilage components separately [11].

At the macroscopic scale, a wide range of studies on AC behavior have been conducted using confined and unconfined compression tests and shear tests. Schinagl et al. [12] performed stress-relaxation confined compression tests on bovine cartilage indentifying heterogeneous elastic properties of the tissue. Newborn bovine patellofemoral groove AC was studied by Ficklin et al. [13] identifying strain dependent AC permeability. A wide spectrum of cartilage moduli from tension to compression was reported in the work of Chahine et al. [14] who performed unconfined compression and tensile tests. The compressive modulus was found nearly constant independently from the direction of load and increasing with the depth, whereas the tensile modulus was strongly affected by both load direction and depth.

The main disadvantages of the tests at macroscale is that the experimental setup can significantly affect the results through misalignments, non-ideal contact conditions between tissue and sample holder and boundary effects which can result in a under- or overestimation of the tissue elastic properties. Nanoindentation is a widely used experimental technique for the analysis of biological tissues in physiological conditions [15,16] with a relatively simple experimental set up. The technique is able to probe small amounts of material with respect to the sample size far from the sample boundaries; therefore, material properties of intact tissue can be obtained.

Nanoindentation can be applied using different sizes for the indenter, opening the possibility to investigate the structure from the whole tissue to the single components. In the work of Jin and Lewis [17], the estimation of the Poisson's ratio was performed using information extracted by two indentations with different tip sizes; in the work of Hu et al. [18], dimensionless relaxation function were introduced from the results of indentation tests carried out with different tips. Oyen et al. [21] have studied the size effect introduced through indentation tests on hydrated tissues as bone and cartilage. They proposed an effective fitting procedure to identify poroelastic and viscoelastic parameters from creep (and relaxation) master curves, and provided a physical interpretation of these parameters with special reference to bone. Park et al. [19] found an effective modulus increasing from 60 kPa to 160 kPa for up to 600 nm of probed depth using a sharp conical tip of radius and opening angle of 50 μm and 35°, respectively. The same depth is investigated with a spherical tip with radius of 2.5 μm, obtaining a modulus that increases from 20 kPa to 40 kPa. Galli et al. [20] used the nano- and microindentation techniques to characterize hydrogels in the time domain as well as in the frequency domain and discussed the time dependence induced by the extrinsic fluid-flow mechanisms in view of the length-scale effects related to the use of different probe sizes.

The aim of this paper is to provide a framework for the quantitative interpretation of the poroelastic response of AC subjected to a multiload spherical indentation test coupled with creep tests. The effect of the probed length and of the tissue strain on the poroelastic tissue response is investigated in detail. Assuming that the dissipation mechanism during creep nanoindentation experiment is primarily of extrinsic nature (i.e., poroelastic), the response at equilibrium, the short term response, and the permeability are investigated through experiments with different tip radii to highlight the dependence on strain. It will be shown that the experimental response is consistent with the above assumption. To this purpose, nanoindentation creep experiments have been also carried out on polydimethylsiloxane (PDMS) samples in dry environment, which are expected to have a time-dependent response of intrinsic nature (i.e., viscoelasticity).

2. Method

2.1. Nanoindentation testing

2.1.1. Samples preparation and instrumentation

AC samples are obtained from lateral and medial condyles of a knee of mature bovine. Three AC samples extracted from neighboring areas of the same bovine knee have been used for testing, one for each of the three test types. Samples harvesting is performed through a biopsy punch with inner diameter of 10 mm. Each explanted plug consisted of a full-thickness AC fragment with its underlying subchondral bone. The plugs are transferred in PBS (2.6 mM NaH_2PO_4, 3 mM Na_2HPO_4, 155 mM NaCl, 0.01% NaN_3 w/v, pH 7.0) supplemented with 20 μg/ml of gentamycin (Invitrogen, Carlsbad, CA, USA,) and a protease inhibitor cocktail (P8340, Sigma, St. Louis, MO, USA) and kept frozen at temperature of −80 °C until measurement; it is assumed the freezing does not affect the behavior of the tissue as described by Kiefer et al. [22].

PDMS disks are obtained mixing viscous components and curing agents with a ratio of 10:1 by weight using the commercial Sylgard 184 Elastomer Kit (Dow Corning, Midland, Michigan, USA). After mixing the two components for at least 5 min, cycles of applied vacuum and rest were carried out to remove all air bubbles. The mixture was then poured in a cylindrical mold of 15 cm of diameter and 0.5 cm of thickness and the PDMS samples were allowed to solidify at 65 °C for 45 min. A biopsy punch with inner diameter of 10 mm was then used to core smaller PDMS samples.

All experiments presented in this work are performed using a NanoTest Indenter (Micro-Materials Ltd., Wrexham, UK) equipped with a liquid cell able to keep samples in a hydrated and fully saturated state (Fig. 1). A 500 mN load cell with a force resolution of 30 nN has been used; the displacement sensor detects penetration depths up to 30 μm with a resolution of 0.1 nm.

Two spherical tips with different radii are used, $R_{400} = 400$ μm and $R_{25} = 25$ μm in the case of cartilage, and $R_{100} = 100$ μm and

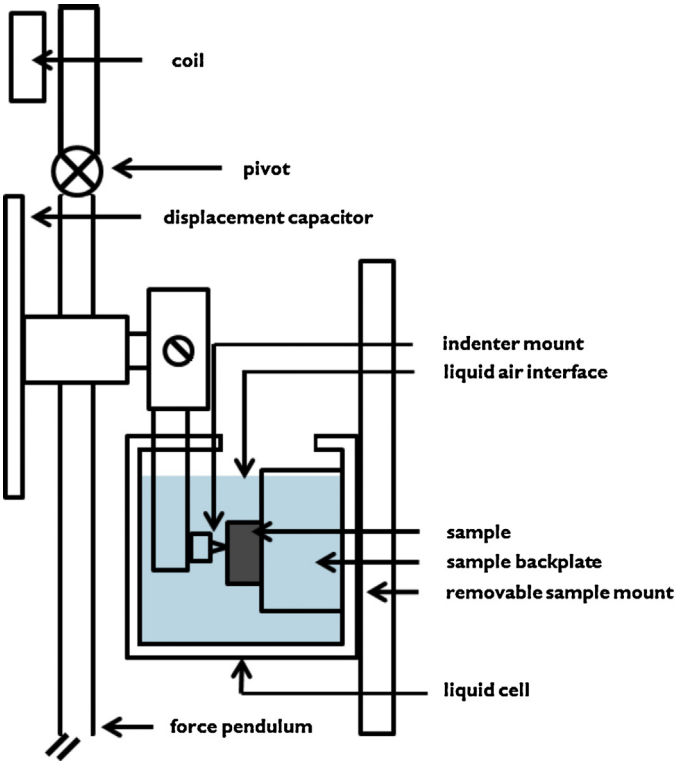

Fig. 1. Sketch of the experimental set-up adopted for the nanoindentation test.

Table 1
Parameters for the experiments carried out on the AC samples.

Sample	Tip radius (μm)	Loading rate (mN/s)	Hold phase (s)	Total load (mN)	Load steps	Repetitions
$C(R_{400}, \nu_1)$	400	1	120	1	10	50
$C(R_{400}, \nu_{10})$	400	10	120	1	10	28
$C(R_{25}, \nu_1)$	25	1	120	1	10	10

R_{25} = 25 μm in the case of PDMS. The same experimental protocol has been used for all tips.

2.1.2. Multiload creep indentation experiments

All cartilage samples were first thawed in a thermal bath at 37 °C for 45 min; then, cyanoacrylate glue was applied to the subchondral bone underlying the AC sample to bond the specimen to the supporting stub and inserted into the liquid cell. The sample was then covered by saline solution (NaCl 0.9% in mass concentration) in order to simulate the realistic conditions of hydration and kept at rest to allow for temperature and swelling equilibrium. Temperature was held at 28 °C for the whole experiment duration. During the experiment, the amount of water is monitored and water refill is performed as necessary to ensure an approximately constant saline concentration in the solution bath.

In the multiload indentation test, the sample is loaded at a prescribed rate until the force value corresponding to the first step is reached; after a holding phase in which a continuous measure of the indentation depth is carried out (creep test), the sample is loaded further to reach the subsequent load level.

The parameters set for the each test are reported in Table 1. The experiments with R_{25} were run using a loading rate of 1 mN/s; the experiments with R_{400} were run with two different loading rates (1 mN/s and 10 mN/s) in order to assess the influence of this experimental parameter on the measured properties. Ten load level and an holding duration of 120 s were considered.

For the case of PDMS, the experiments have been performed in dry conditions with the setup reported in Table 2.

All tests were conducted by an automatic procedure on a preselected spatial grid. Each spot of the grid defines a repetition (one multiload cycle). Due to surface defects, the surface detection procedure may in same cases fail; data of these experiments were discarded and the number of acceptable repetitions has been listed in each table: a lower limit of 10 repetitions have been considered large enough to have significant statistics. On PDMS samples, a grid of 10 repetitions was scheduled as no surface detection errors occurred.

2.2. 1-D interpolation function for the indentation test

As in the work of Hu et al. [18] in which 1-D phenomenological interpolation functions are proposed to fit force history data of relaxation nanoindentation tests, a 1-D interpolation function is proposed in this work for the multiload creep tests. The selection of the fitting function is made on the basis of the solution to the problem of the surface settlement of a poroelastic material layer resting on a stiff impermeable base subjected to constant surface loading, also regarded as consolidation problem. Indeed, no closed form solutions are available for spherical poroelastic nanoindentation problems; Mak et al. [23] proposed a numerical solution for the flat punch indentation which is obtained by using double Laplace and Hankel transform.

According to the solution proposed by Biot [24] and extended to the case of finite ramp time [25], using the notation as in Cowin and Doty [8], the vertical displacement of the top surface of the poroelastic layer $u(t)$ in a consolidation problem, can be written as:

$$u(t) = u^u(0) + u^t(t) = u^u(0) + \overline{P_1} g(\tau) \tag{1}$$

with

$$g(\tau) = 1 - \sum_{m=0}^{\infty} \frac{8}{(1+2m)^4 \pi^4 \tau_R} [e^{-(1+2m)^2 \pi^2 (\tau - \tau_R)} - e^{-(1+2m)^2 \pi^2 \tau}] \tag{2}$$

where the parameter $\overline{P_1}$ depends on the elastic properties of the material. A dimensionless time parameter τ can be introduced; for confined compression tests, Galli and Oyen [25] use $\tau = (ct)/4L^2$ where t is the physical time and c is a diffusivity parameter which is proportional to the tissue permeability and stiffness. Parameter τ_R is the dimensionless time at $t = t_R$ where t_R is the duration of the loading ramp.

Eq. (1) is recast in the multiload nanoindentation problem to obtain the displacement history during creep at the jth load level $h^j(\tau)$ by means of the two parameters fitting function:

$$h^j(\tau) = h^j(0) + \overline{P_1^j}[g(\tau^j)] \tag{3}$$

where $h^j(0)$ is the indentation depth at the beginning of the creep phase of the j-th load level. Moreover, a new dimensionless time τ is defined for any of the load levels in analogy to that introduced by Oyen et al. [21]:

$$\tau^j = \frac{\overline{P_2^j} t}{\beta^2 a^2} = \frac{\overline{P_2^j} t}{\beta^2 R h^j(t)} \tag{4}$$

in which two characteristic lengths for spherical indentation have been introduced: the radius of the spherical indenter, R, and the displacement during the hold phase $h^j(t)$, with $\overline{P_1^j}$ and $\overline{P_2^j}$ the two fitting parameters. In Eq. (3), the characteristic fluid path length $\bar{a} = \beta a$, proportional to the contact radius ($a \sim \sqrt[2]{R h^j(t)}$) is used; $\beta = 2.86$ is identified as shown in the Supplementary Material. The parameter $\overline{P_1^j}(h)$ (nm) is the difference between the displacement in the drained ($t \to \infty$) and that in the undrained ($t \to 0$) condition. $\overline{P_2^j}(h)$ (nm^2/s) $= AkM_d$, having the same physical units of c, acts as a diffusivity parameter which depends on the drained indentation modulus M_d, on the permeability k, and on the parameter A. For isotropic poroelasticity and assuming an undrained Poisson's ratio $\nu_u = 0.5$, A becomes $A = (1-\nu_d)^2/(1-2\nu_d)$ [18] [21]. In the range $\nu_d = [0.05 - 0.25]$ as identified by Oyen et al. [21], A varies in the range [1.002–1.125], therefore, in this work it has been assumed $A = 1$.

Table 2
Parameters for the experiments carried out on the PDMS samples.

Sample	Tip radius (μm)	Loading rate (mN/s)	Hold phase (s)	Total load (mN)	Load steps	Repetitions
$P(R_{25}, \nu_1)$	25	1	120	1	10	10
$P(R_{100}, \nu_1)$	100	1	120	1	10	10

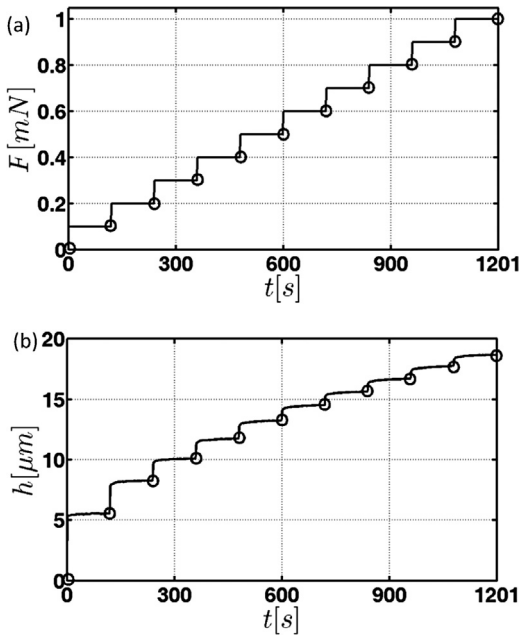

Fig. 2. (a) Force vs time: ten load steps from 0 mN to 1 mN have been applied with load increments of 0.1 mN; (b) typical displacement in function of time data recorded during the whole experiment. Open circles indicate the end of the creep phase at each load level.

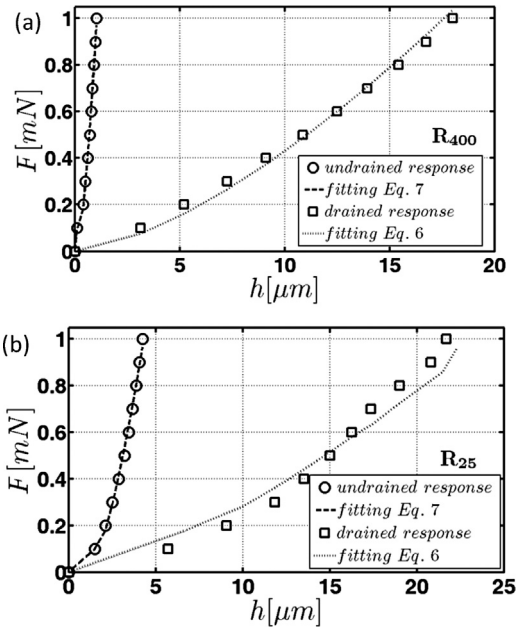

Fig. 3. (a) A representative experimental result for the undrained (circle) and the drained (square) response for $C(R_{400}, \nu_1)$ and the best fitting lines using Eqs. (6–7). (b) A representative experimental result for the undrained (circle) and the drained (square) response for $C(R_{25}, \nu_1)$ and the best fitting lines using Eqs. (6–7).

2.3. Data analysis

The output data at each load level F_L^j of the experimental tests are:

1. The drained, h_d^j, and the undrained, h_u^j, displacement. The drained indentation depth is the indentation depth measured at the end of the j-th creep phase $h_d^j = h^j(t = 120\ \text{s})$ and it represents the tissue response in drained (equilibrium) condition. The undrained displacement is obtained as a summation of undrained displacement increments $\Delta h_u^k : h_u^j = \sum_{k=1}^{j} \Delta h_u^k(F_L^k)$, where $\Delta h_u^k(F_L^k) = h^k(t = 0) - h^{k-1}(t = 120\ \text{s})$.
2. The time-domain data $h^j(t)$ which is the displacement history measured for each j-th load level during the holding phase.

Following the theory of spherical indentation of a purely elastic half space, the static load-indentation $(F-h)$ relationship is [26] [27]:

$$F = \frac{4}{3} E^* \sqrt[2]{R} h^{3/2} \tag{5}$$

where, E^* is the indentation modulus of the deformable body and R is the radius of the indenter. Eq. (5) can be used to fit the $(F_L - h_d)$ and $(F_L - h_u)$ data points to identify the drained (M_d) and the undrained (M_u) indentation modulus as follows:

$$F_L = \frac{4}{3} M_d \sqrt[2]{R} {h_d}^{3/2} \tag{6}$$

$$F_L = \frac{4}{3} M_u \sqrt[2]{R} {h_u}^{3/2} \tag{7}$$

The symbols F_L, h_d, and h_u without superscript j indicate the vectors that collect all the ten levels of force, drained displacement and undrained displacement of a single multiload test: $F_L = [F_L^j]_{j=1}^{10}$, $h_d = [h_d^j]_{j=1}^{10}$ and $h_u = [h_u^j]_{j=1}^{10}$. Fig. 2 shows a representative force history and displacement response for the R_{400} tip radius; Fig. 3 shows a typical result for the drained and the undrained responses, along with the relative best fittings (using Eqs. (6) and (7)), for experiments performed with the R_{400} tip radius (Fig. 3(a)) and the R_{25} tip radius (Fig. 3(b)); Fig. 4 shows the creep response for a representative ten levels test for $C(R_{400}, \nu_1)$. Under the assumption that a steady state at the end of each load level is achieved, creep curves are mutually independent, allowing to scale time in the range 0–120 s for all load levels. The effect of the load ramp is accounted for by the known parameter $h^j(0)$ for each creep curve.

For PDMS samples, the modulus computed using data at the end of the creep phases is the long term modulus $M_{lt} = M(t \to \infty)$.

Applying a best fitting procedure on the experimental curves $h^j(t)$ using Eq. (3), the parameters $\overline{P_1}$ and $\overline{P_2}$ can be identified. By using the definition of $\overline{P_2}$ a value for the depth-dependent permeability can be estimated as

$$k^j = \frac{\overline{P_2^j}(h)}{M_d} \tag{8}$$

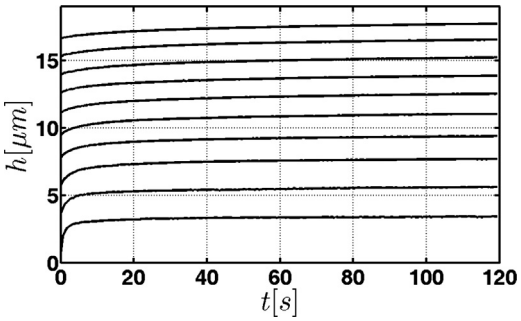

Fig. 4. Example of ten different creep curves related to the ten increasing loads in the range 0.1–1 mN.

Table 3
Values of M_d and M_u for AC samples reported as mean value and standard deviation. Range of variation of goodness fit parameter R^2 is also reported.

Sample	Drained modulus M_d (MPa)			Undrained modulus M_u (MPa)		
	Mean	Std dev	R^2	Mean	Std dev	R^2
$C(R_{400}, v_1)$	0.50	0.15	0.97–0.99	40	8	0.97–0.99
$C(R_{400}, v_{10})$	0.49	0.41	0.97–0.98	234	63	0.96–0.99
$C(R_{25}, v_1)$	1.74	0.41	0.93–0.98	25	1	0.95–0.99

The consolidation ratio is introduced to normalize the indenter displacement:

$$\overline{h^j} = \frac{(h^j(t) - h_d^j)}{(h_u^j - h_d^j)} \tag{9}$$

According to the Herzian contact theory, the contact radius, l_c^j, which is an estimate of the characteristic length of the experiments is

$$l_c^j = \sqrt[2]{2Rh^j - h^{j2}} \tag{10}$$

An equivalent indentation strain, ε_{eq}^j, as proposed by Lin et al. [28] and verified by other authors [29,30], is here introduced:

$$\varepsilon_{eq}^j = \frac{l_c^j}{R} \tag{11}$$

The above definition was introduced by Tabor [31] for metals, but the work of Lin et al. [28] suggests that it is applicable also to the indentation on soft biological tissues. Then, Eq. (11) defines a scalar representative measure of the inhomogeneous strain distribution beneath the indenter surface and it is correlated with the increase in length of material fiber with respect to its undeformed length.

The commercial code MATLAB (MathWorks, Natick, MA, USA) and the constrained interior-point algorithm is used in a least square framework to find the optimum parameters.

3. Results

3.1. Articular cartilage

All the curves $(F_L - h_d)$ and $(F_L - h_u)$ measured for each of the three types of experiments (50, 28 and 10 repetitions, respectively) were subjected to a best fitting procedure using Eqs. (6) and (7) to estimate the drained modulus M_d and the undrained modulus M_u, respectively. The mean values and the standard deviations computed for these three cases are shown in Table 3 along with the range of variation of the goodness of fit parameter R^2. The indentation modulus obtained with the 25 μm tip (1741 ± 41 kPa) is higher than that obtained with the 400 μm indenter 500 kPa. They differ in a non-parametric unpaired Mann–Whitney–Wilcoxon test at a significance level $\alpha < 0.01$. No size dependence is observed in the undrained modulus which have no statistical difference for $\alpha < 0.05$. To assess the effect of the loading rate, tests were carried out with the larger tip ($C(R_{400}, v_1)$ and $C(R_{400}, v_{10})$) at two different rates: 1 mN/s and 10 mN/s. As expected, a significant effect is found on the undrained response whereas no statistical difference ($\alpha < 0.01$) was found on the equilibrium (drained) response. In all cases, undrained moduli are significantly higher than the drained ones.

The high values of the R^2 found in all cases show that the hypothesis of Hertzian contact is acceptable for both drained and undrained conditions [32], for which a purely elastic behavior can be expected.

The bar graphs presented in Fig. 5 compare the data collected in Table 3, by separating the effects of tip radius and loading rate. Fig. 5(a) presents the values of M_d when the sample is tested at the same loading rate, but with different tip radii (samples $C(R_{400}, v_1)$ and $C(R_{25}, v_1)$); in Fig. 5(b), instead, M_u is reported when the sample is tested with the same tip radius, but at different loading rates (samples $C(R_{400}, v_1)$ and $C(R_{400}, v_{10})$). The black bars indicate the standard deviations.

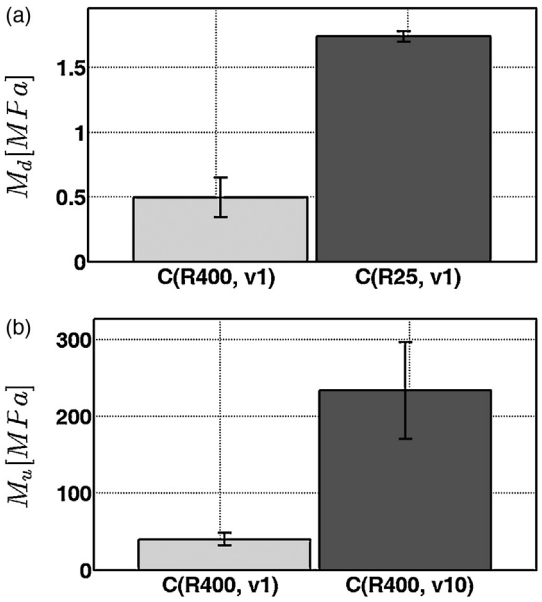

Fig. 5. (a) Drained moduli for the cases of different tips and same loading rate. (b) Undrained moduli for the cases of same tip and different loading rates. Mean and standard deviation are presented.

Figs. 6 and 7 present, respectively, the drained and undrained moduli as a function of the equivalent deformation (Figs. 6(a) and 7(a)) and the contact radius (Figs. 6(b) and 7(b)). Means and standard deviations are reported, and the horizontal lines indicate the maximum and minimum indentation strain/contact radius achieved during the experiments. An increasing indentation modulus with increasing representative

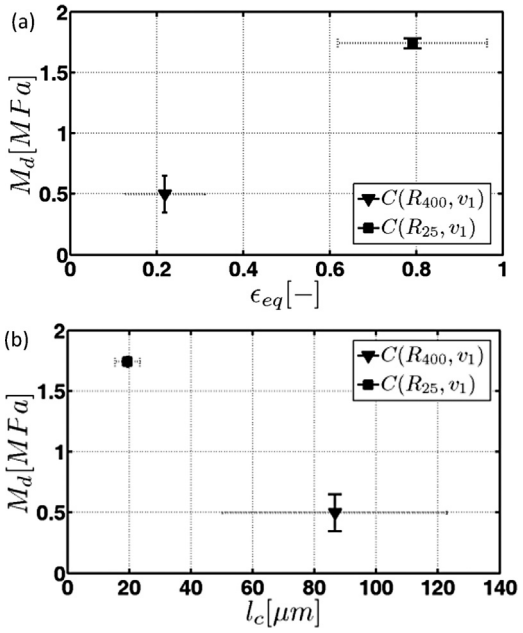

Fig. 6. (a) Drained moduli vs the equivalent indentation strain. (b) Drained moduli vs the contact radius. Mean (marker) standard deviation (solid line) are presented as well as the range of both the parameters analyzed into a single multiload test (dot line). Only tests carried out at the same loading rate are reported.

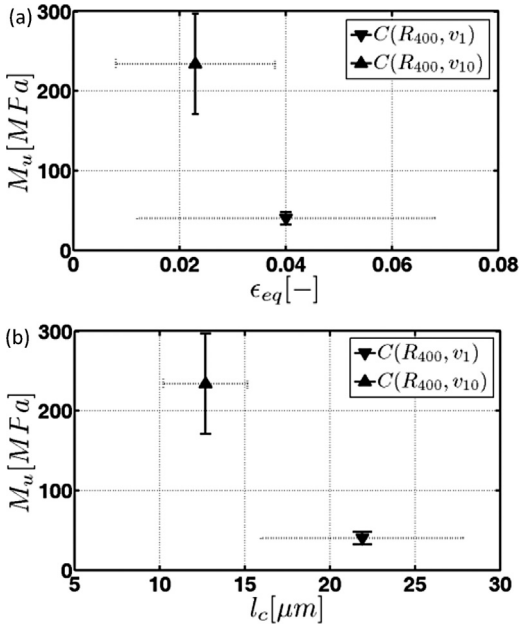

Fig. 7. (a) Undrained moduli vs to the equivalent indentation strain. (b) Undrained moduli vs to the contact radius. Mean (marker) standard deviation (solid line) are presented as well as the range of both the parameters analyzed into a single multi-load test (dot line). Only tests carried out with the same tip are reported.

indentation strain is found, whereas a decreasing modulus is found for an increasing characteristic length.

Fig. 8(a) reports the values of permeability (mean and standard deviation) computed as a function of equivalent deformation for all the load levels; considering the experimental data obtained with same loading rate 1 mN/s and the different tip radii $C(R_{400}, v_1)$ and $C(R_{25}, v_1)$, this curve show the well-known strain-dependent behavior and it is fitted according to [36]

$$k(\varepsilon) = k_0 e^{-k_1 \varepsilon} \tag{12}$$

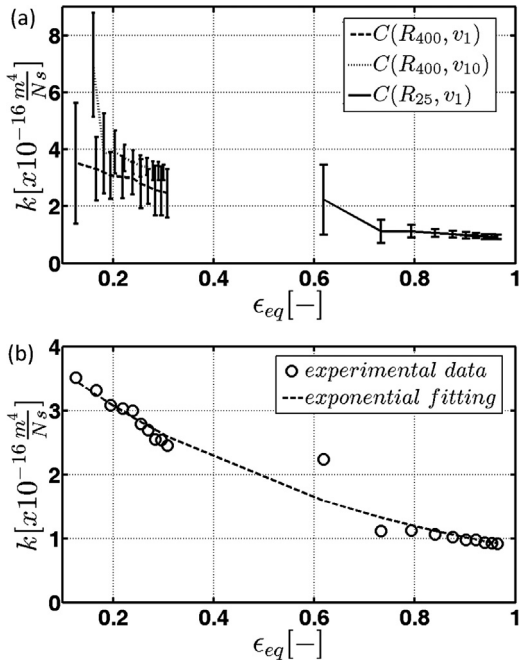

Fig. 8. (a) Permeability with respect to the indentation strains. (b) Fitting of strain-dependent permeability using Eq. (12).

Table 4
Values of M_{lt} for PDMS samples as mean value and standard deviation. Range of variation of goodness fit parameter R^2 is also reported.

Sample	Long term modulus M_{lt} (MPa)		
	Mean	Std dev	R^2
$P(R_{25}, v_1)$	3.77	0.08	0.96–0.99
$P(R_{100}, v_1)$	3.72	0.07	0.97–0.99

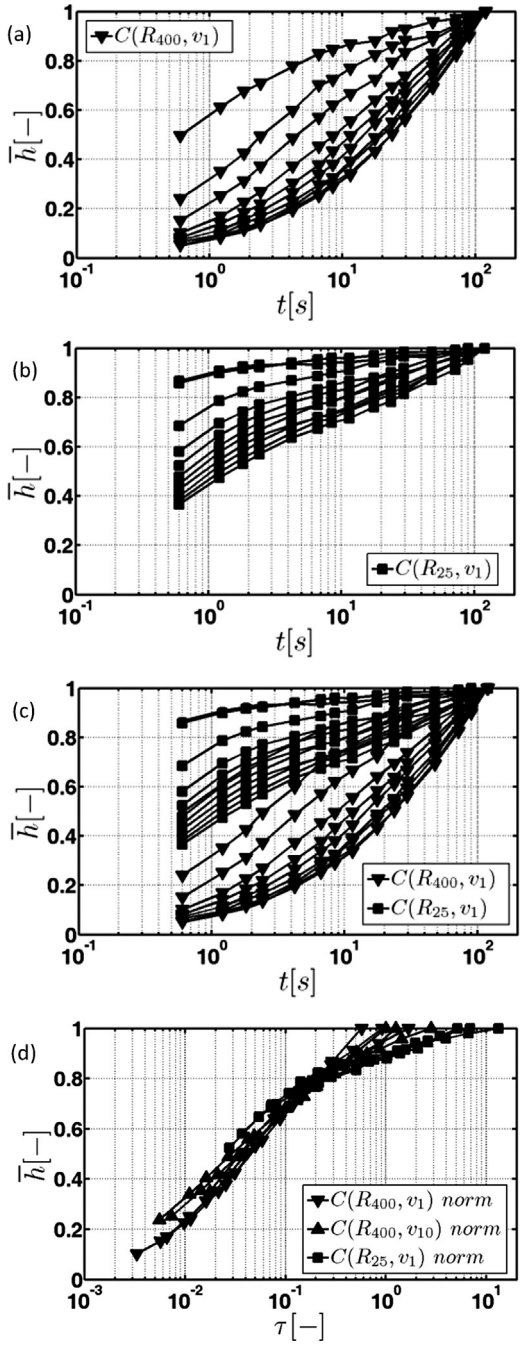

Fig. 9. (a) Consolidation ratio curves for representative 10 load levels for the experiment $C(R_{400}, v_1)$ in function of natural time. (b) Consolidation ratio curves for representative 10 load levels for the experiment $C(R_{25}, v_1)$ in function of natural time. (c) Curves in (a) and (b) are plotted together. (d) Selected consolidation ratio curves in dependence of normalized time for all the three cases analyzed for AC samples.

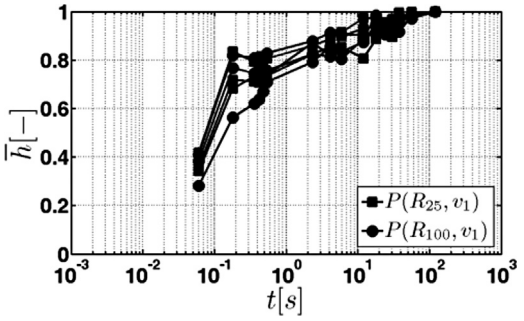

Fig. 10. Normalized indentation depth plotted in dependence of natural time for PDMS samples. For the different tip radii and loading condition, only representative curves are presented.

where k_0 and k_1 are two fitting parameters. Fig. 8(b) shows the result of the best fitting procedure, with $k_0 = 4.2 \times 10^{-16}$ m^4/Ns and $k_1 = 1.6$.

3.2. PDMS

Table 4 shows the values of the long term indentation moduli calculated for the PDMS samples. No statistical differences at $\alpha < 0.01$ are found between the results collected with the two tips indicating that the long term response for PDMS is independent of the indenter radius.

3.3. Time-dependent response of AC and PDMS samples under nanoindentation

Fig. 9(a) reports the consolidation ratio for ten representative levels of load using the R_{400} tip. As expected for a fluid filled solid under a constant load, the consolidation rate is greater for smaller characteristic sizes; i.e., for increasing load, the contact area increases and the time required to achieve a given consolidation ratio increases. The characteristic size of the indentation can be changed by changing the tip radius. In Fig. 9(b), the consolidation ratio is reported for all load levels using the R_{25} tip. The time response under multiload creep is qualitatively similar to the response obtained with the large tip, but consolidation is considerably faster for the smaller tip as shown in Fig. 9(c).

Following the theoretical solution of the consolidation problem, if the normalized time, one for each load level, is considered (Eq. (4)), $\overline{h_F^j}$ becomes independent of the characteristic size. R^2 values for all curves fitting the creep data range between 0.8 and 0.99 for the large radius tip, and between 0.7 and 0.95 for the small radius tip.

If consolidation curves are reported as a function of normalized time for all load levels and for all tip radii, no appreciable difference can be observed as shown in Fig. 9(d), where the consolidation curves for all the studied cases overlap.

As a comparison, Fig. 10 shows representative curves of the time-dependent response to a constant indentation load for PDMS in dry conditions: the normalized consolidation rate $\overline{h_F^j}$ as a function of time t overlaps within the experimental scattering for all characteristic lengths; this shows that the time-dependent phenomenon is independent on the contact radius of the experiments with PDMS samples. This results indicates that indentation on PDMS in dry condition is mostly an intrinsically viscoelastic phenomenon.

4. Discussions and conclusions

The behavior of the superficial layers of AC derives from the spatial organization of its different constituents [33]. In this work, we focused on the effects of the characteristic length of the nanoindentation experiment on the time-dependent response of AC in a physiological (i.e., liquid) environment. The analyses allowed us at identifying drained and undrained indentation modulus, as well as the tissue permeability. Effects of characteristic lengths were investigated by performing indentation tests with spherical tips with two different radii and different penetration depths by setting a multiload procedure. The penetration depths achieved in all experiments were lower than 25 μm, therefore it was assumed independence of the results from through-the-thickness inhomogeneity.

The value of drained modulus obtained with the small tip (R_{25}) is three times higher than that found with the large tip (R_{400}). This effect was also found in Simha et al. [34] where the drained indentation modulus of bovine patellar cartilage decreased up to three times (from 4.5 MPa to 1.5 MPa) with increasing indenter radius from 0.1 mm to 1 mm. Simha attributed this result to the spatial heterogeneities as well as to the different amount of AC tissue probed with different tips. The tests carried out with the small tip cover a wide range of high equivalent deformations ($\varepsilon_{eq} \in [0.61–0.96]$) and small characteristic contact sizes ($l_c \in [15–23]$ μm). Vice versa, those conducted with the large tip investigate a range of smaller equivalent deformation ($\varepsilon_{eq} \in [0.12–0.31]$) with large contact sizes ($l_c \in [50–125]$ μm). According to Fig. 6, the drained indentation modulus increases with increasing applied equivalent deformation, as seen at the macroscale with unconfined compression tests [35], and decreases with increasing contact radius. These two results suggest that the drained modulus increases if smaller volume of tissue (i.e., smaller amount of AC collagen fibrils) are recruited and loaded at high strain.

The value of the undrained modulus increases substantially if the loading rate increases, as shown in Fig. 5(b) (results for $C(R_{400}, v_1)$) (see also Table 3). At a given loading rate, the undrained modulus is not dependent on the tip radius and on the equivalent strain as no statistical difference was found between the 400 μm and the 25 μm tip. This suggests that, unlike the drained response, the short term tissue response is weakly related to the material microstructure; it is rather owed to the fluid pressure increase upon sudden loading.

Using the analytical solution for a 1-D consolidation problem, an estimation of the tissue permeability at different equivalent deformations can be carried out. As a result of the Finite Element validation step, one single diffusivity parameter, able to simulate creep data at all load levels for both spherical tip radii, has been found. This is an indication that the 1-D fitting function is appropriate for this particular experiment and that the parameters are correlated with indentation modulus and permeability, as stated in Hu et al. [18].

Nia et al. [37] found an average permeability of 10^{-14} m^4/Ns on immature bovine cartilage samples by a dynamic atomic force microscopy based nanoindentation; Chen et al. [38] found permeability, extrapolated at zero compressive strain, of 4.55×10^{-15} m^4/Ns on superficial layers of adult bovine cartilage samples using confined compression experiments. The tissue permeability predicted in this study (Fig. 8(b)) is lower than that found in [37,38]; the permeability obtained with the larger sphere at the first load level is about two times larger than that found by Oyen et al. [21] with a spherical tip of radius 239 μm at an indentation depth of 3.4 μm ($l_c \sim 40$ μm). This suggests that experimental conditions and tissue sources should be carefully accounted for when making consistent comparison between tissue permeability measures obtained in different studies. Furthermore, Williamson et al. [39] have shown that tissue permeability is strain-dependent (they found values in the range 10^{-15}–10^{-17} m^4/Ns for compressive strains ranging from 0.15 to 0.45) as well as age-dependent, finding decreasing permeability with tissue age, especially at large strains.

Critical issues for this model and potential limitations are briefly discussed in the following. The time-dependent response has been recorded over a time span of 120 s. The choice of 120 s as holding time is a compromise between the total duration of the whole experiment and the need to achieve an equilibrium configuration (total dissipation of the excessive pore pressure). Indeed, the testing apparatus is not suited for longer holding time because of the increasing effect of thermal drift with the experiment duration and the fixed number of sampling points recordable during the creep phases. A short creep phase could overestimate the drained modulus. Nevertheless, in order to check the achievement of a steady state configuration with a good accuracy, the numerical time derivative of the creep displacement as a function of time has been computed on average creep curves for each indenter radius and each loading level. The worst condition was found for the case $C(R_{400}, \nu_1)$ at the 10th load level, for which a creep displacement rate of 4 nm/s was computed. Considering that the creep rate decreases with time, the additional creep displacement that would be accumulated for $t > 120$ s is expected to be below the experimental variability. The additional creep displacement that would be accumulated during the load levels from 1st to 9th is even lower because lower creep rates are measured for those levels. As expected, creep rates at 120 s calculated for the 25 μm tip experiments are lower than that found for the 400 μm tip; therefore, the underestimation of the long term creep displacement has a very limited effect on the estimation of the drained indentation modulus found for the 25 μm tip.

The creep tests carried out in this work can be partially affected by the finite duration of the loading ramp, i.e., no step loading is applied. This issue has been accounted for in the estimation of the tissue permeability by using the fitting Eq. (2), which is similar to that used in Galli and Oyen [25]. The function (2) explicitly accounts for the duration of the loading ramp. The tissue permeability estimated with the R_{400} tip and two different loading rates is the same (see Fig. 8a), to within the experimental variability, except of the first load level (Fig. 8a): this is a clear indication that the effect of the loading ramp has been correctly accounted for.

For comparison purposes, the same experimental protocol has been applied on PDMS samples in dry conditions which are expected to be homogeneous and intrinsically viscoelastic. Fig. 10 shows that PDMS has a prevalent viscoelastic behavior. Indeed, normalized creep curves (normalized displacement vs. natural time) obtained at different indentation loads overlap, i.e., they do not exhibit size dependence [40].

Unlike PDMS, the time response of cartilage can be explained through the poroelastic dissipation mechanism. Fig. 9 suggests that, at least at the time scales investigated in this study, poroelasticity is the main phenomenon governing AC superficial zone. The size dependence observed using two different tip radii and different penetration depths is shown by plotting normalized displacement vs. time. If the normalized displacement is plotted against the normalized time (Eq. (7)), all curves overlap, i.e., the size dependence disappears.

Both viscoelasticity and poroelasticity have to be taken into account when hydrated tissues with fibril networks are investigated at macroscopic characteristic lengths since both interstitial fluid flow and collagen fibril bending affect the overall response (i.e., under confined compression tests [41]). Although macroscopic indentation testing is suitable to investigate poroviscoelastic parameters, Galli et al. [42] showed that analyzing the data by assuming linear poroelasticity leads to an overestimate of permeability. Our finding on AC is corroborated by Gupta et al. [43] who confirmed that viscoelasticity of the fibers plays an important role in the macroscopic tensile response of articular cartilage, but it was ignored in their nanoindentation experiments, since the effect of fluid pressurization prevails when compression is the dominant mode of deformation [44]. Besides, Oyen et al. [21] suggested that a poroviscoelastic theory would be more suitable if AC is investigated at characteristic lengths larger than ~220 μm, that is twice the maximum characteristic length analyzed in this work.

It can be expected that the intrinsic viscoelastic behavior of collagen fibrils as well as of the other molecular components of cartilage solid matrix may also play a role. However, as the typical fibril diameter is 20–80 nm, viscous dissipation should be detectable for characteristic lengths much smaller than those investigated in this work and on larger time scales. It can be speculated that AFM-based indentation using a sharp tip radius and low applied loads may be more suitable to probe the viscoelastic response of cartilage fibrillar component.

Anisotropy is also an important issue on cartilage mechanics. However, the aim of this work is to characterize tissue stiffness through the indentation modulus and no specific reference has been made to the single components of the elastic tensor and their relationship with the indentation modulus [45,46]. Limiting to the case of a transversely isotropic material subjected to an axisymmetric indentation, the indentation modulus along the axis of symmetry (direction 3 in the following equation) can be analytically written as [46]

$$M_t = 2\sqrt[2]{\frac{C_{31}^2 - C_{13}^2}{C_{11}}\left(\frac{1}{C_{44}} + \frac{2}{C_{31} + C_{13}}\right)^{-1}} \tag{13}$$

where $C_{11} = C_{1111}$, $C_{13} = C_{1133} = C_{3311}$, $C_{44} = C_{2323} = C_{1313}$, $C_{33} = C_{3333}$ and $C_{31} = \sqrt[2]{C_{11}C_{33}}$. C_{ijhk} is the generic coefficient of the material fourth order stiffness tensor, where i,j,h,k = [1–3].

Our study introduces two significant innovations. (i) We probed different characteristic lengths at the same spot of the tissue, thus allowing to circumvent the uncertainties due to the intrinsic spatial variability of the tissue; (ii) we used fitting functions derived from the analytical solution of a poroelastic problem, although with different boundary conditions, and validated them through finite element analyses; the specific boundary conditions involved in the spherical indentation problem have been partially accounted for by introducing the geometrical parameter β estimated through the FEM simulation. Two potential applications with clinical relevance can be envisioned. Multiload nanoindentation tests on human physiologic and pathologic samples would allow to quantitatively assess microscopic tissue stiffness and permeability at different pathology stages. Furthermore, the proposed method can be used to quantify the biomechanical compatibility of engineered tissue substitutes before implantation.

Funding

Italian Ministry of University and Research, through the PRoject of National Interests program (PRIN2008), RiMED Foundation fellowship for RG.

Ethical approval

Not required.

Appendix A. Supplementary data

Supplementary data associated with this article can be found, in the online version, at http://dx.doi.org/10.1016/j.medengphy.2014.03.008.

Conflict of interest

No conflict of interest.

References

[1] Raviv U, Giasson S, Kampf N, Gohy J, Jerome R, Klein J. Lubrication by charged polymers. Nature 2003;425:163–5.
[2] Mow V, Ratcliffe A, Poole A. Cartilage and diarthroidal joints as paradigms for hierarchical material and structure. Biomaterials 1992;13(2):67–97.
[3] Wilson W, van Donkelaar C, Huyghe J. A comparison between mechano, electrochemical and biphasic swelling theories for soft hydrated tissues. J Biomech Eng 2005;127:158–65.
[4] Terzaghi V. Theoretical soil mechanics. New York: Wiley; 1943.
[5] Biot M. Theory of elasticity and consolidation for a porous anisotropic solid. J Appl Phys 1955;26(2):182–5.
[6] Rice J, Cleary M. Some basic stress diffusion solution for fluid-saturated elas-tic porous media with compressible constituents. Rev Geophys Space Phys 1976;14:227–41.
[7] Coussy O. Poromechanics. England: John Wiley & Sons; 2004.
[8] Cowin S, Doty S. Tissue mechanics. New York: Springer Verlag; 2006.
[9] Armstrong C, Lai W, Mow V. An analysis of the unconfined compression of articular cartilage. J Biomed Eng 1984;106:165–73.
[10] Cohen B, Lai W, Mow V. A transversely isotropic biphasic model for unconfined compression of growing plate and chondroepihysis. J Biomech Eng 1998;120:491–6.
[11] Lu X, Wan L, Guo X, Mow V. A linearized formulation of triphasic mixture theory for articular cartilage and its application to indentation analysis. J Biomech 2010;43(4):673–9.
[12] Schinagl R, Gurskis D, Chen A, Sah R. Depth-dependent confined com-pression modulus of full thickness bovine articular cartilage. J Orthop Res 1997;15(4):499–506.
[13] Ficklin T, Thomas G, Barthel J, Thonar E, Masuda K, Asanbaeva A, et al. Articular cartilage mechanical and biochemical property relations before and after in vitro growth. J Biomech 2007;40(16):3607–14.
[14] Chahine N, Wang C, Hung C, Ateshian G. Anisotropic strain-dependent material properties of bovine articular cartilage in the transitional range from tension to compression. J Biomech 2004;37(8):1251–61.
[15] Ebenstein D, Pruitt L. Nanoindentation of biological materials. Nano Today 2006;1:26–33.
[16] Li L, Korhonen R, Iivarinen J, Jurvelin J, Herzog W. Fluid pressure driven fibril reinforcement in creep and relaxation tests of articular cartilage. Med Eng Phys 2008;30:182–9.
[17] Jin H, Lewis J. Determination of Poisson's ratio of articular cartilgae by indentation using different-sized indenters. J Biomech Eng 2004;126(2):138–45.
[18] Hu Y, Zhao X, Vlassak J, Suo Z. Using indentation to characterize the poroelasticity of gels. Appl Phys Lett 2010;96, 121904-1:3.
[19] Park S, Duong C, Lee J, Lee S, Son K. Effect of tip geometry of atomic force microscope on mechanical responses of bovine articular cartilage and agarose gel. Int J Precis Eng Manuf 2010;11(1):129–36.
[20] Galli M, Comley K, Shean T, Oyen M. Viscoelastic and poroelastic mechanical characterization of hydrated gels. J Mater Res 2009;24(3):973–9.
[21] Oyen M, Shean T, Strange D, Galli M. Size effect in indentation of hydrated biological tissues. J Mater Res 2012;27(1):245–55.
[22] Kiefer G, Sundby K, McAllister D, Shrive N, Frank C, Lam T, et al. The effect of cryopreservation on the biomechanical behavior of bovine articular cartilage. J Orthop Res 1989;7:495–501.
[23] Mak A, Lai W, Mow V. Biphasic indentation of articular cartilage—I. Theoretical analysis. J Biomech 1987;20(7):703–14.
[24] Biot M. General theory of three dimensional consolidation. J Appl Phys 1941;12:155–64.
[25] Galli M, Oyen M. Fast identification of poroelastic parameters from indentation tests. CMES – Comp Model Eng Sci 2009;48:241–68.
[26] Johnson K. Contact mechanics. Cambridge/Oxford/New York: Cambridge University Press/Clarendon Press/Oxford University; 1985.
[27] Field J, Swain M. A simple predictive model for spherical indentation. J Mater Res 1993;8:297–306.
[28] Lin D, Dimitriadis E, Horkay F. Elasticity of rubber-like materials measured by AFM nanoindentation. eXPRESS Polym Lett 2007;1(9):576–84.
[29] Iwashita N, Swain M, Field J, Ohta N, Bitoh S. Elasto-plastic deformation of glass-like carbons heat-treated at different temperatures. Carbon 2011;39: 1525–32.
[30] Briscoe B, Fiori L, Pelillo E. Nano-indentation of polymeric surfaces. J Phys D: Appl Phys 1998;19:2395–405.
[31] Tabor D. Hardness of metals. Clarendon Press; 1951.
[32] Dintwa E, Tijskens E, Ramon H. On the accuracy of the Hertz model to describe the normal contact of soft elastic spheres. Granul Matter 2008;10:209–21.
[33] Jurvelin J, Muller D, Wong M, Studer D, Engel A, Hunziker E. Surface and subsurface morphology of bovine humeral articular cartilage as assessed by atomic force and transmission electron microscopy. J Struct Biol 1996;117: 45–54.
[34] Simha N, Jin H, Hall M, Chiravarambath S, Lewis J. Effect of indenter size on elastic modulus of cartilage measured by indentation. J Biomech Eng 2007;129:767–75.
[35] Li L, Buschmann M, Shirazi-Adl A. Strain-rate dependent stiffness of articular cartilage in unconfined compression. J Biomech Eng 2003;125:161–8.
[36] Ateshian G, Warden W, Kim J, Grelsamer R, Mow V. Finite deformation biphasic material properties of bovine articular cartilage from confied compression experiments. J Biomech 1997;30:1137–64.
[37] Nia H, Han L, Li Y, Ortiz C, Grodzinsky A. Poroelasticity of cartilage at the nanoscale. Biophys J 2011;101:2304–13.
[38] Chen A, Bae W, Schinagl R, Sah R. Depth- and strain-dependendent mechanical and electromechanical properties of full-thickness bovine articular cartilage in confined compression. J Biomech 2001;34(1):1–12.
[39] Williamson A, Chen A, Sah R. Compressive properties and function-composition relationships of developing bovine articular cartilage. J Orthop Res 2001;19:1113–21.
[40] Hu Y, Chen X, Whitesides G, Vlassak J, Suo Z. Indentation of polydimethylsiloxane submerged in organic solvents. J Mater Res 2011;26:785–95.
[41] Chandran P, Barocas V. Microstructural mechanics of collagen gels in con-fined compression: poroelasticity, viscoelasticity, and collapse. J Biomech Eng 2004;126:152–66.
[42] Galli M, Fornasiere E, Cugnoni J, Oyen M. Poroviscoelastic characterization of particle-reinforced gelatin gels using indentation and homogenization. J Mech Behav Biomed Mater 2011;4:610–7.
[43] Gupta S, Lin J, Ashby P, Pruitt L. A fiber reinforced poroelastic model of nanoindentation of porcine costal cartilage: a combined experimental and finite element approach. J Mech Behav Biomed 2009;2:326–38.
[44] Li L, Herzog W. Electromechanical response of articular cartilage in indentation – considerations on the determination of cartilage properties during arthroscopy. Comput Method Biomech 2005;8(2):83–91.
[45] Taffetani M, Bertarelli E, Gottardi R, Raiteri R, Vena P. Modelling of the frequency response to dynamic nanoindentation of soft hydrated anisotropic materials: application to articular cartilage. CMES – Comp Model Eng Sci 2012;87(5):433–60.
[46] Delafargue A, Ulm F. Explicit approximations of the indentation modulus of elastically orthotropic solids for conical indenters. Int J Solids Struct 2004;41:7351–60.